Studies on Melt Spinning. VIII. Transfer Function Approach

SUSUMU KASE and MASASHI ARAKI, *Kyoto University of Industrial Arts and Textile Fibers (KOSENDAI), Sakyoku Matsugasaki, Kyoto 606, Japan*

Synopsis

Transfer function analyses were carried out on a linearized perturbation model of melt spinning previously developed. Results are as follows. (1) Formal proof was obtained of the criterion of spinline stability stated in terms of transfer function. (2) A new concise statement of the stability criterion was obtained: the spinline is stable when the transfer function $G_2(s)$ connecting the spinline tension to the spinline velocity does not have a zero in the right-hand half of the complex s plane. (3) Effects of various external disturbances on filament unevenness were predicted theoretically by expressing the transfer function between each disturbance input and cross-sectional area at take-up in the form of frequency response Bode diagrams.

INTRODUCTION

A number of reports are now available on the mathematical analysis of spinline transients. One can refer to the reviews by Petrie and Denn,[1] Denn,[2] White and Ide,[3] Ziabicki,[4] and Petrie,[5] among others. So far, transients in melt spinning have been studied from two major points of view. One is spinline stability, and the other is sensitivity.

The problem of sensitivity concerns the conditions under which spinlines taken up at constant speed become unstable to develop draw resonance, a severe sustained oscillation in cross-sectional area and tension.

Sensitivity concerns the quantitative dynamic effects of various disturbance inputs to the spinline on filament quality. One such example is the effect of time-dependent cooling air speed on the unevenness of the filament cross-sectional area.

In the present work, the authors introduce a formal proof to the criterion of spinline stability stated previously without full proof by Kase and co-workers[6–8] and go on to develop a systematic computation procedure for the theoretical prediction of the effects of external disturbances on filament unevenness.

Transfer function analysis of spinline sensitivity has been described in a conference proceedings[8] and in an unpublished in-house report.[9] To the authors' knowledge, however, the present work is the first full article devoted to this subject. The definition and major attributes of transfer function are reviewed in the Appendix.

GOVERNING EQUATIONS

The transfer function analyses in the present work are based on the mathematical model of melt spinning developed by Kase and Matsuo[10] and subse-

Journal of Applied Polymer Science, Vol. 27, 4439–4465 (1982)
 CCC 0021-8995/82/114439-27$03.70

quently slightly extended by Kase.[7] The model consists of a set of simultaneous partial differential equations, eqs. (1) through (13), reproduced from the literature with some changes:

Continuity

$$\frac{\partial A}{\partial t} + \frac{\partial}{\partial x}(Av) = 0 \tag{1}$$

Momentum

$$\frac{\partial F}{\partial x} = 0 \tag{2}$$

Power law constitutive

$$\frac{\partial v}{\partial x} = \left(\frac{F}{\beta A}\right)^{1/n} \tag{3}$$

Energy

$$\frac{\partial T}{\partial t} + v\frac{\partial T}{\partial x} = \frac{2\sqrt{\pi}h(T^* - T)}{C_p \rho \sqrt{A}} \tag{4}$$

Temperature vs. viscosity

$$\beta = \beta_\infty \left(e^{E/T+273} + \frac{B}{T-60}\right) \tag{5}$$

Heat transfer correlation

$$\mathrm{Nu} = 0.42R_e^{\,0.333}\left\{1 + \left(\frac{8v_y}{v}\right)^2\right\}^{0.167} \tag{6}$$

Nusselt number definition

$$\mathrm{Nu} = \frac{hd}{k_{\mathrm{air}}} = \frac{2h\sqrt{A}}{k_{\mathrm{air}}\sqrt{\pi}} \tag{7}$$

Reynolds number definition

$$\mathrm{Re} = \frac{vd}{\nu_{\mathrm{air}}} = \frac{2v\sqrt{A}}{\nu_{\mathrm{air}}\sqrt{\pi}} \tag{8}$$

Kinetic viscosity of air

$$\nu_{\mathrm{air}} = 0.290\ \mathrm{cm^2/s} \tag{9}$$

Heat conductivity of air

$$k_{\mathrm{air}} = 0.808 \times 10^{-4}\ \mathrm{cal/cm \cdot s \cdot C} \tag{10}$$

In eqs. (1) through (10), x is distance from the spinneret, t is time, A is local filament cross-sectional area, v is local filament speed, F is spinline tension, T is filament temperature, β is tensile viscosity, n is power law exponent, h is heat transfer coefficient at filament surface, ρ is polymer density, C_p is specific heat of the polymer, d is filament diameter, E is activation energy, B is a constant equal to 100, ν_{air} is the kinetic viscosity of air, and k_{air} is the heat conductivity of air. Units are in cgs, except for tension F and viscosity β, which are expressed in gram force (see Fig. 1).

The material constant β_∞ is the tensile viscosity at $T = \infty$ and is an attribute

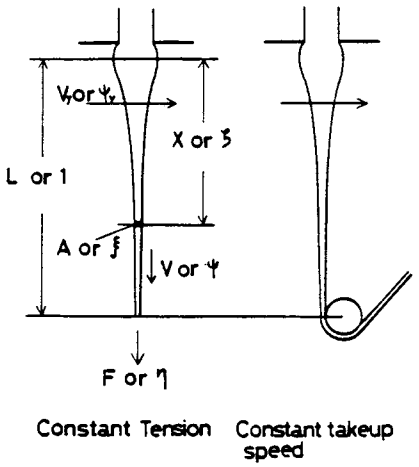

Fig. 1. Schematic of melt spinning.

somewhat resembling the intrinsic viscosity of the polymer. In the present mathematical spinline model, β_∞ of the polymer emerging from the spinneret hole is allowed to vary with time around its steady-state value $\bar{\beta}_\infty$.

$$\beta_\infty(t') = \beta^*(t')\bar{\beta}_\infty \tag{11}$$

Note that β_∞ and the dimensionless factor β^* are functions of spinneret time t' rather than the present time t; t' is the time a particular fluid element now ($t = t$) located at $x = x$ has left the spinneret. The cross blow air speed v_y and ambient air temperature T^* are, in general, functions of distance x.

Simplifying assumptions made in deriving the above governing equations are:

(1) Purely extensional local flow field.
(2) Newtonian viscosity and its dependence on temperature alone.
(3) Constant polymer density ρ and specific heat C_p.
(4) Constant $\bar{\beta}_\infty$, E, ν_{air}, and k_{air}.
(5) Uniform temperature and velocity v over filament cross section.
(6) Neglect of viscous dissipation in the energy equation.
(7) Neglect of heat conduction in the axial direction.
(8) Inclusion of radiant heat transfer in the convective heat transfer coefficient h.
(9) Neglect of extrudate swell effects.
(10) Neglect of inertia, surface tension, gravity, and air drag.

Boundary conditions at the spinneret are:

$$\begin{aligned} &A = A_{00} = \text{const.} \qquad v = v_{00} = \text{const.} \\ &T = T_{00} \text{ const.} \qquad \text{at } x = 0 \end{aligned} \tag{12}$$

The downstream boundary condition of constant take-up speed is

$$v = v_w = \text{const.} \qquad \text{at } x = L \tag{13}$$

A boundary condition alternative to eq. (13) is to specify spinline tension $F(t)$ as given *a priori* (see Fig. 1).

$$F(t) = \text{any function of time given } a \textit{ priori} \tag{14}$$

The only unspecified parameter values $\bar{\beta}_\infty$ and E in the above governing equations can be determined experimentally following the procedure below:

(1) Experimentally measure $A(x)$, $T(x)$, and F under a representative steady-state spinning condition.

(2) Substitute the measured $A(x)$, $T(x)$, and F into eq. (16) below to obtain a $\beta(T)$ correlation:

$$Av = A_{00}v_{00} = \text{const.} \qquad \beta^*(t) = 1 \tag{15}$$

$$\beta(x) = -\frac{FA}{A_{00}v_{00}} \Big/ \frac{dA}{dx} \tag{16}$$

Equations (15) and (16) can be derived from eqs. (1) and (3) assuming steady state.

(3) Determine the values of $\bar{\beta}_\infty$ and E by fitting the above experimental $\beta(T)$ correlation with eq. (5) considering eqs. (11) and (15).

These $\bar{\beta}_\infty$ and E values based on experimental data taken in a single steady-state spinning were found[10,11] to lead to both steady-state and transient solutions of the governing equations that reasonably agree with experimental measurements over a wide range of spinning conditions.

For general discussion, we further render the above governing equations dimensionless by defining the dimensionless variables in Greek characters:

$$x = \zeta L \qquad t = \tau L/v_\infty \qquad A = \xi A_\infty \qquad v = \psi v_\infty$$
$$T = \theta T_\infty \qquad t' = \tau' L/v_\infty \qquad v_y = \psi_y v_\infty$$
$$T^* = \theta^* T_\infty$$

$$F = \frac{A_{00}v_{00}\bar{\beta}_{00}\left(e^{E/(T_{00}+273)} + \dfrac{B}{T_{00}-60}\right)}{L} \tag{17}$$

Substitution of coefficient correlations (5) to (11) into eqs. (1) to (4) reduces the number of equations from 11 to 4. By further substituting eqs. (17) into the resultant 4 equations, the governing equations reduce to the dimensionless form below ready for analytical or numerical solution:

Continuity

$$\frac{\partial \xi}{\partial \tau} + \frac{\partial}{\partial \zeta}(\xi\psi) = 0 \tag{18}$$

Momentum

$$\frac{\partial \eta}{\partial \zeta} = 0 \tag{19}$$

Newtonian constitutive

$$\left(\frac{\partial \psi}{\partial \zeta}\right)^n = \frac{\eta\left(e^{E/(T_{00}+273)} + \dfrac{B}{T_{00}-60}\right)}{\beta^*\xi\left(e^{E/(T_{00}\theta+273)} + \dfrac{B}{T_{00}\theta-60}\right)} \tag{20}$$

Energy

$$\frac{\partial\theta}{\partial\tau} + \psi\frac{\partial\theta}{\partial\zeta} = -St\,\xi^{-0.833}\psi^{0.333} \times \left\{1 + \left(8\frac{\psi y}{\psi}\right)^2\right\}^{0.167}(\theta - \theta^*) \tag{21}$$

where

$$St = 1.67 \times 10^{-4}\,\rho^{-1}C_p{}^{-1}A_{00}{}^{-0.833}v_{00}{}^{-0.667}L \tag{22}$$

Note that in an isothermal spinning, filament temperature T is everywhere equal to spinneret temperature T_{00} to make θ equal to unity. This in turn simplifies the right-hand side of eq. (20) to $\eta/(\beta^*\xi)$. Also in isothermal spinning, ambient air temperature θ^* is equal to filament temperature θ. Therefore, both sides of eq. (21) are zero, causing the energy eq. (21) to drop out of the governing equations.

Upstream boundary conditions at the spinneret are

$$\xi = \psi = \theta = 1 \qquad \text{at } \zeta = 0 \tag{23}$$

and the downstream boundary condition of constant take-up speed is

$$\psi = \psi_w = v_w/v_{00} = \text{const.} \qquad \text{at } \zeta = 1 \tag{24}$$

where ψ_w is the steady-state drawdown ratio.

STEADY-STATE SOLUTION

The procedure to compute the steady-state solution of the dimensionless governing eqs. (18) through (21) is essentially identical to the steady-state solution of eqs. (1) through (4) discussed previously[10,12] by one of the present authors. One simply sets the time derivative $\partial/\partial\tau$ equal to zero and solves eqs. (18) and (21) as simultaneous ordinary differential equations.

First of all, at steady state the continuity eq. (18) reduces to

$$\xi\psi = 1 \tag{25}$$

to enable the elimination of velocity ψ from the governing equations. Further, in the special case of isothermal spinning, the energy eq. (21) drops out of the governing equations as discussed above to yield an analytical steady-state solution, eq. (26) for Newtonian fluids ($n = 1$) below, in which subscript zero denotes the steady state and ψ_w is the drawdown ratio defined in eq. (24):

$$\xi_0(\zeta) = 1/\psi_0 = \psi_w{}^{-\zeta} \tag{26}$$

Equation (26) is a straight line on a semilog graph.

In most cases, other than the above numerical computation is required to obtain the steady-state solution. Usually, a simple first-order backward differencing scheme suffices to obtain a reasonably precise solution at minimal computer time requirement. It should be noted that spinline tension η constitutes a part of the solution to be determined in a Newton–Raphson iteration scheme to satisfy the downstream boundary condition, eq. (24). In most cases, the solution converges in three or four iterations. In the present work, a computer program called MS3 developed in a previous work[7] was used to compute the steady-state solutions. The program allows cooling air temperature θ^* and

cooling air speed ψ_y to vary with distance ζ, though θ^* and ψ_y were considered constants in the present work.

PERTURBATION ABOUT STEADY STATE

As was discussed in detail previously,[7,10] the governing eqs. (18) through (21) can be linearized about the steady state to obtain a set of perturbation equations. In linearizing the governing equations, the perturbation variables $\hat{\xi}$, $\hat{\psi}$, $\hat{\theta}$, $\hat{\psi}_y$, $\hat{\beta}$, and $\hat{\eta}$ are defined below in Greek letters:

$$\begin{aligned} \xi(\tau,\zeta) &= \xi_0(\zeta)\{1 + \hat{\xi}(\tau,\zeta)\} \\ \psi(\tau,\zeta) &= \psi_0(\zeta)\{1 + \hat{\psi}(\tau,\zeta)\} \\ \psi_y(\tau,\zeta) &= \psi_{y0}(\zeta)\{1 + \hat{\psi}_y(\tau,\zeta)\} \\ \theta(\tau,\zeta) &= \theta_0(\zeta)\{1 + \hat{\theta}(\tau,\zeta)\} \\ \beta^*(\tau') &= 1 + \hat{\beta}(\tau') \\ \eta(\tau) &= \eta_0\{1 + \hat{\eta}(\tau)\} \end{aligned} \tag{27}$$

In eqs. (27), subscript zero denotes the steady state. When eqs. (27) are substituted into eqs. (18) to (22) and the second- and higher-order terms in the perturbation variables are ignored, the perturbation eqs. (28) through (30) below are obtained for the Newtonian case of $n = 1$:

Continuity

$$\frac{\partial\hat{\xi}}{\partial\tau} + \frac{\partial\hat{\xi}}{\partial\zeta^*} + \frac{\partial\hat{\psi}}{\partial\zeta^*} = 0 \tag{28}$$

Constitutive plus momentum

$$\frac{\partial\hat{\psi}}{\partial\zeta^*} = f_1(\hat{\eta} - \hat{\psi} - \hat{\xi} - \hat{\beta}) + f_2\hat{\theta} \tag{29}$$

Energy

$$\frac{\partial\hat{\theta}}{\partial\tau} + \frac{\partial\hat{\theta}}{\partial\zeta^*} = f_3\hat{\xi} + f_4\hat{\psi} + f_6\hat{\theta} - f_5\hat{\psi}_y \tag{30}$$

$$\zeta^* = \int_0^{\zeta} \xi_0(\zeta)\, d\zeta = \int_0^{\zeta} d\zeta/\psi_0(\zeta) \tag{31}$$

The variable ζ^* defined in eq. (31) above is the steady-state residence time in the region bounded by $\zeta = 0$ and $\zeta = \zeta$. The use of ζ^* in place of ζ as distance variable greatly simplifies the perturbation equations since it eliminates the scale conversion factor ψ_0 between time and distance.

Coefficients f_1 through f_6 are all functions of ζ^* and are respectively equal in expression to the $f_1(z)$ through $f_6(z)$ given previously[7,10] when each of the latter is multiplied by the factor L/v_∞ to make them dimensionless. It is quite significant that coefficients f_1 through f_6 are completely determined by the steady-state solution, $\xi_0(\zeta)$ and $\theta_0(\zeta)$, of the nonlinear governing eqs. (18) through (21).

Upstream boundary conditions for the perturbation equations under no disturbance to the spinneret are

$$\hat{\xi} = \hat{\psi} = \hat{\theta} = 0 \qquad \text{at } \zeta^* = 0 \tag{32}$$

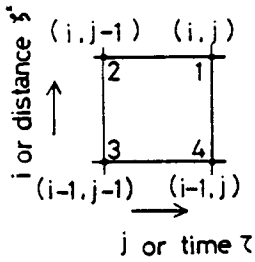

Fig. 2. Differencing mesh for the solution of perturbation equations.

and the downstream boundary condition of constant take-up speed is when the take-up is undisturbed:

$$\hat{\psi} = 0 \qquad \text{at } \zeta^* = \zeta_w^* = \int_0^1 d\zeta \Big/ \xi_0(\zeta) \tag{33}$$

The initial condition is

$$\hat{\xi} = \hat{\psi} = \hat{\theta} = 0 \qquad \text{at } \tau = 0 \tag{34}$$

for transients starting from steady state. A boundary condition alternative to eq. (34) is

$$\hat{\eta} = 0 \qquad \text{or} \qquad \hat{\eta} = u(\tau) = \text{unit step function} \tag{35}$$

representing spinlines subject to constant tension (see Fig. 1).

Throughout the present study, a unit step increase in $\hat{\eta}$ or $\hat{\psi}_y$ or one of $\hat{\xi}$, $\hat{\psi}$, $\hat{\theta}$, and $\hat{\beta}$ at the spinneret ($\zeta^* = 0$) were considered as disturbance inputs to the linearized spinline model. As eqs. (11) and (27) show, extrusion viscosity perturbation $\hat{\beta}$ is a function of spinneret time τ', which happens to be

$$\tau' = \tau - \zeta^* \tag{36}$$

in the perturbation model.

Since the numerical solution of the perturbation eqs. (28) to (30), though in dimensioned form, was discussed in detail previously,[7,10] just an outline of the solution procedures is given below.

The latter half of program MS3 is devoted to the transient solution of perturbation eqs. (28) to (30). Program MS3 derives coefficients $f_1(\zeta^*)$ through $f_6(\zeta^*)$ from the steady-state solution computed in the first half of the program in the form of a table and proceeds to solve eqs. (28) to (30) for transients.

The partial derivatives in eqs. (28) to (30) were approximated by first-order backward differencing along the 45-degree characteristic line shown in Figure 2 to obtain a set of differencing equations. Integers i and j are increment numbers in the direction of τ and ζ^*, respectively, and ω is any one of the dependent variables.

$$\frac{\partial \omega}{\partial \tau} + \frac{\partial \omega}{\partial \zeta^*} = \frac{\omega_{i,j} - \omega_{i-1,j-1}}{\Delta} \tag{37}$$

$$\frac{\partial \omega}{\partial \zeta^*} = \frac{\omega_{i,j} - \omega_{i-1,j}}{\Delta} \tag{38}$$

$$\Delta = \Delta\tau = \Delta\zeta^* \tag{39}$$

Under this differencing scheme, the values of dependent variables at point 1, or the (i, j) point in Figure 2, can each be expressed as an explicit function of the values of dependent variables at points 3 and 4. This enables a consecutive marching computation of all mesh points in one time step when tension perturbation $\hat{\eta}$ is specified as given. However, when the downstream boundary condition of constant take-up speed must be met, tension perturbation $\hat{\eta}$ is determined in a Newton–Raphson iteration process to satisfy eq. (35).

Shown in Figure 3 are two different responses of cross-sectional area $\hat{\xi}$ at take-up position $\zeta^* = \zeta_w^*$ to a unit-step increase in extrusion viscosity:

$$\hat{\beta} = u(\tau') = u(\tau - \zeta_w^*) \tag{40}$$

as computed by means of program MS3 and drawn automatically by a X–Y plotting machine without human intervention in data handling. Time scale is in multiples of the steady-state residence time ζ_w^* to the take-up point defined in eq. (33) rather than in time τ itself.

Parameter values used in computing the two curves in Figure 3 and throughout the rest of this paper, unless stated otherwise, are as listed below.

$$\rho = 0.83\ \text{g/cm}^3 \quad C_p = 0.7\ \text{cal/g} \cdot \text{deg} \quad T^* = 20°\text{C}$$
$$T_\infty = 270°\text{C} \quad A_\infty = 5.641 \times 10^{-4}\ \text{cm}^2 (d = 0.0268\ \text{cm at } x = 0)$$

$$v_w = 1000\ \text{m/min} = 1667\ \text{cm/s} \quad v_y = 30\ \text{cm/s} \tag{41}$$
$$\bar{\beta}_\infty = 0.040\ g_f\text{s/cm}^2 \quad E = 3500\ \text{deg} \quad B = 100\ \text{deg}$$
$$n = 1 \quad \Delta = \zeta_w^*/400$$

From (41) above,

$$\psi_w = 52.67 \quad \psi_y = 0.9478 \quad \theta^* = 0.1111 \tag{42}$$

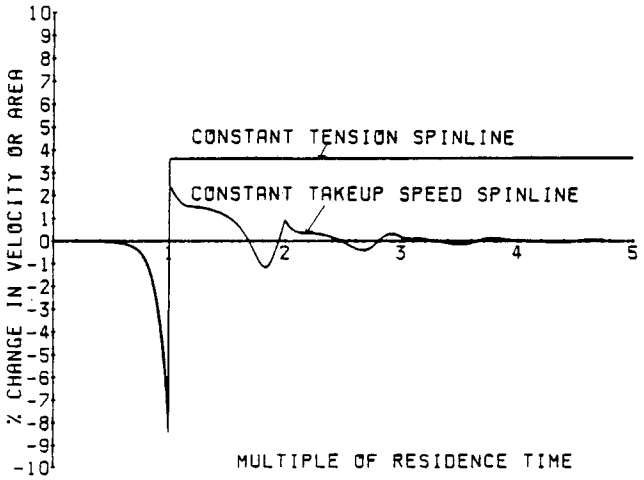

Fig. 3. Transient linearized response of the take-up cross-sectional area to unit (1%) step increase in extrusion viscosity. Both under constant take-up speed and constant tension.

The spinning conditions given in (41) and (42) above are for a typical low-speed melt spinning of polypropylene filament.

The lower $\hat{\xi}(\zeta_w^*, \tau)$ curve in Figure 3, eventually tending to zero, is for the downstream boundary condition of constant take-up speed given in eq. (33); and the upper $\hat{\xi}(\zeta_w^*, \tau)$ curve that reaches a new steady state at the elapse of one steady-state residence time α_w^* is for the boundary condition of constant spinline tension $\hat{\eta} = 0$ as given in eq. (35).

In fact, for isothermal spinlines of Newtonian and power law fluids subjected to stepwise increase in extrusion viscosity under the boundary condition of constant tension, analytical transient solutions are available[13] for both perturbation eqs. (18) to (21) and nonlinear governing eqs. (28) to (30) and the perturbation solution reaches a new steady state in one steady state residence time ζ_w^* and the nonlinear solution in a certain finite time.

Solution of nonlinear governing eqs. (18) to (21):

Disturbance input: $$\beta^*(\tau') = 1 + \beta^{**}\, u(\tau') \tag{43}$$

Initial steady state: $$\xi = \psi_w^{-\zeta} \quad \text{when } \tau \le 0 \tag{44}$$

Transient: $$\xi = (1 - \tau \log\psi_w)\left(1 - \frac{\tau \log \psi_w}{1 + \beta^{**}}\right)^{-(1+\beta^{**})} \cdot \psi_w^{-\zeta}$$

when $$0 < \tau < \frac{1 + \beta^*}{\log \psi_w}\{1 - \psi_w^{-\zeta/(1+\beta^{**})}\} = \tau_{\text{end}} \tag{45}$$

Second steady state: $$\xi = \psi_w^{-\zeta/(1+\beta^{**})}$$

when $$\tau > \tau_{\text{end}} \tag{46}$$

Solution of perturbation eqs. (28) to (30):

Disturbance input: $$\hat{\beta} = u(\tau') \tag{47}$$

Initial steady state: $$\hat{\xi} = 0 \quad \text{when } \tau < 0 \tag{48}$$

Transient:
$$\hat{\xi} = -\log(1 - \tau \log \psi_w) - \frac{\tau \log \psi_w}{1 - \tau \log \psi_w}$$

when $$0 < \tau < \frac{1 - \psi_w^{-\zeta}}{\log \psi_w} = \tau_{\text{end}}$$

where $$\zeta = \log(1 + \zeta^* \log \psi_w) \tag{49}$$

Second steady state: $$\hat{\xi} = \zeta \log \psi_w \quad \text{when } \tau > \tau_{\text{end}} \tag{50}$$

Equations (46) and (50) do not contain time τ to show that the spinline has reached a new steady state. At present, the authors are not able to show analytically that the transient is confined to the region OAC in Figure 4 under the general nonisothermal conditions. However, the reasoning below shows that this is exactly the case.

Referring to the schematic in Figure 5, point B is the present location of the fluid element which left the spinneret hole A at time $\tau = 0$ when the stepwise

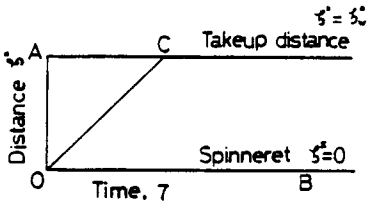

Fig. 4. Solution domain: distance ζ^* (= steady-state residence time) vs. time τ.

increase in extrusion viscosity occurred. Spinline tension $\hat{\eta}$ is the only medium which can convey the effects of deformation taking place in one part of the spinline to another, whereas, under the boundary condition of constant tension, this medium cannot function. Therefore, the deformation of the spinline between points A and B under constant tension is independent of that below point B, the AB part thus necessarily being in a new steady state under the new spinning conditions defined by the step disturbance input. This confines the transient deformation to the part of the spinline below point B corresponding to the region OAC in Figure 4. In other words, the spinline at a certain distance from the spinneret enters the new steady state as soon as the viscosity border B goes past that point.

The fact that constant-tension spinlines always settle to a new steady state after a stepwise disturbance precludes their chance of experiencing any growing or sustained oscillation to make them always stable. This gives a physical explanation to the inherent stability of constant-tension spinline, first discovered by Pearson and Matovich.[14]

Both the nonlinear and linear solutions shown in eqs. (43) to (50) indicate that a stepwise downward-facing area discontinuity develops at the border B between the high and low viscosities, as shown in Figure 5, with the discontinuity growing as point B flows down the spinline. In fact, this area discontinuity corresponds to the jump in $\hat{\xi}(\zeta_w^*, \tau)$ shown in Figure 3.

COMPUTATION OF TRANSFER FUNCTIONS

When $y(\tau)$ is the output signal emerging from the linearized spinline model in eqs. (28) to (30) in response to an input signal $z(\tau)$, then the transfer function

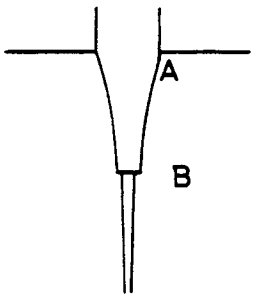

Fig. 5. Spinline side profile after a stepwise increase in extrusion viscosity.

$G(s)$ representing that particular dynamic input–output relation is

$$G(s) = \mathcal{L}\{y(\tau)\}/\mathcal{L}\{z(\tau)\} \tag{51}$$

as discussed in Appendix A. Further, when $z(\tau)$ is a unit step function, eq. (51) becomes

$$G(s) = \mathcal{L}\{y(\tau)\}/\mathcal{L}\{u(\tau)\} = s\mathcal{L}\{y(\tau)\} \tag{52}$$

or, in the frequency domain,

$$\begin{aligned} G(j\omega) &= j\omega \int_0^\infty e^{-j\omega\tau} y(\tau)\, d\tau \\ &= \omega \int_0^\infty (\sin \omega\tau) y(\tau)\, d\tau + j\omega \int_0^\infty (\cos \omega\tau) y(\tau)\, d\tau \end{aligned} \tag{53}$$

In principle, therefore, $G(j\omega)$ can be numerically computed by solving the perturbation eqs. (28) to (30) for the response $y(\tau)$ of the linearized spinline model to a unit step disturbance input $u(\tau)$ and by Laplace transformation of the output $y(\tau)$ by means of eq. (53).

In practice, however, precise Laplace transformation becomes difficult when the step response $y(\tau)$ takes a long time to converge to a fixed value, as in the lower curve in Figure 3 for the constant take-up speed spinline. Furthermore, when the spinline is unstable, step response $y(\tau)$ becomes a diverging oscillation, rendering the numerical Laplace transformation in eq. (53) impossible.

Fortunately, these difficulties can be avoided by means of an alternative method[8] of computing $G(s)$ in which $G(s)$ is decomposed into four transfer functions $G_1(s)$ through $G_4(s)$ associated with constant-tension spinline, which is known to be always stable.

The first step in the alternative method is to replace the constant-speed take-up roll with a constant-tension device while keeping other conditions unchanged (see Fig. 1). The block diagram in Figure 6 shows the dynamics of the constant-tension spinline thus obtained. Considered in Figure 6 are two input signals, extrusion viscosity $\hat{\beta}(\tau')$ and spinline tension $\hat{\eta}(\tau)$, and two output signals, cross-sectional area $\hat{\xi}(\zeta_w, \tau)$ and velocity $\hat{\psi}(\zeta_w, \tau)$, both at take-up distance ζ_w. Input signal $\hat{\beta}(\tau')$ can be replaced by any other input signal and $\hat{\xi}(\zeta_w, \tau)$, by any other output signal without affecting the validity of the present discussion. It is always possible to numerically compute the four transfer functions $G_1(j\omega)$ through $G_4(j\omega)$ since the constant-tension spinline they represent is always stable. Considering that the step response $y(\tau)$ always settles to a constant value H at $\tau = \zeta_w$ under constant tension, the integrations in eq. (53) can be broken down into two parts to obtain eq. (54):

$$\begin{aligned} G_i(j\omega) = \int_0^{\zeta_w} (\sin \omega\tau)\, y(\tau)\, d\tau + j\omega \int_0^{\zeta_w} (\cos + \omega\tau)\, y(\tau)\, d\tau \\ + H(\cos \omega\zeta_w - j \sin \omega\zeta_w) \end{aligned} \tag{54}$$

A highly accurate numerical Laplace transformation is possible with eq. (54) since, unlike in eq. (53), the numerical integration in eq. (54) is over the short range from $\tau = 0$ to $\tau = \zeta_w$.

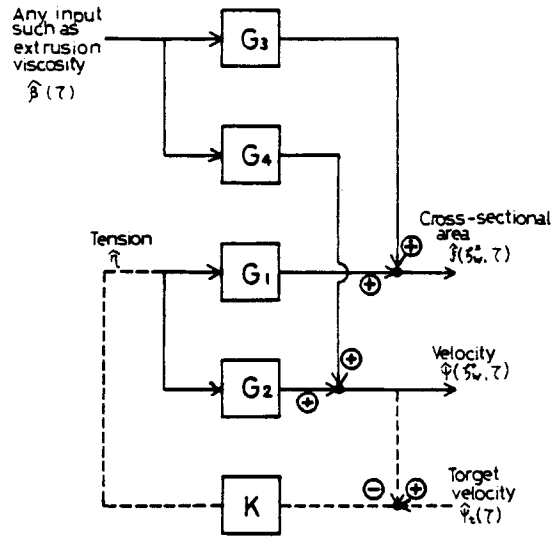

Fig. 6. Feedback mechanism that realizes the constant-speed take-up.

The next step in computing $G(j\omega)$ is to consider an imaginary negative feedback loop[8] shown as dotted lines in Figure 6. In the feedstock loop, the take-up point velocity $\hat{\psi}(\zeta_w^*, \tau)$ is subtracted from an arbitrarily given target velocity $\hat{\psi}_t(\tau)$ to obtain the error $\hat{\epsilon}(\tau)$ which in turn is multiplied by a constant gain factor K to become tension perturbation $\hat{\eta}(\tau)$. The feedback loop is thus essentially an automatic control system which detects the spinline velocity at take-up position $\zeta^* = \zeta_w^*$ and tries to bring the velocity $\hat{\psi}(\zeta_w^*, \tau)$ to the target velocity $\hat{\psi}_t(\tau)$ by varying the spinline tension in proportion to the error $\hat{\epsilon}(\tau)$. With the feedback loop, the Laplace transforms of $\hat{\epsilon}(\tau)$ and $\hat{\xi}(\zeta_w^*, \tau)$ are expressed as

$$\mathcal{L}\{\hat{\epsilon}(\tau)\} = \frac{-G_4\mathcal{L}\{\hat{\beta}(\tau')\} + \mathcal{L}\{\hat{\psi}_t(\tau)\}}{1 + KG_2} \tag{55}$$

$$\mathcal{L}\{\hat{\xi}(\zeta_w^*, \tau\} = \left(G_3 - \frac{KG_1G_4}{1 + KG_2}\right)\mathcal{L}\{\hat{\beta}(\tau')\} + \frac{KG_1}{1 + KG_2}\mathcal{L}\{\hat{\psi}_t(\tau)\} \tag{56}$$

Equation (55) above shows that error $\hat{\epsilon}(\tau)$ tends to zero as feedback gain K goes to infinity to make the velocity $\hat{\psi}(\zeta_w^*, \tau)$ at take-up distance coincide with the target velocity $\hat{\psi}(\tau)$.

$$\hat{\psi}(\zeta_w^*, \tau) \equiv \hat{\psi}_t(\tau) \qquad \text{when } K = \infty \tag{57}$$

Further, when the target velocity $\hat{\psi}_t(\tau)$ is equal to zero or a constant, an infinitely large K brings about a constant take-up speed spinline. Then, eq. (56) reduces to eq. (58):

$$\mathcal{L}\{\hat{\xi}(\zeta_w^*, \tau)\} = \left(G_3 - \frac{G_1G_4}{G_2}\right)\mathcal{L}\{\hat{\beta}(\tau')\} + \frac{G_1}{G_2}\mathcal{L}\{\hat{\psi}_t(\tau)\} \tag{58}$$

The transfer function G between extrusion viscosity $\hat{\beta}(\tau')$ and take-up cross-sectional area $\hat{\xi}(\zeta_w^*, \tau)$ is therefore

$$G = G_3 - \frac{G_1 G_4}{G_2} \tag{59}$$

and that between target velocity $\hat{\psi}_t(\tau)$ and $\hat{\xi}(\zeta_w, \tau)$ is

$$G = \frac{G_1}{G_2} \tag{60}$$

Equations (59) and (60) are two examples of decomposing a transfer function G representing a constant take-up speed spinline into transfer functions G_1 through G_4 representing a constant tension spinline. In Eq. (58) above, $\hat{\beta}(\tau')$ can be replaced by any other disturbance input variable and $\hat{\xi}(\zeta_w, \tau)$, by any other output variable without changing the form of the equation. Equations (54), (59), and (60) enable the expression of $G(s) = G(j\omega)$ in a frequency domain Bode diagram or in a vector locus.

Three computer programs, DMS, DMA, and PLT, were developed to respectively carry out the Laplace transformation in eq. (54), the vector arithmetic in eq. (59) or eq. (60), and the automatic drawing or a Bode diagram or a vector locus to record the computed $G(j\omega)$. Later, the above three programs were combined serially together with MS3 to form a single TSS program TRANS, having 1770 Fortran statements. Thus, merely giving spinning conditions to TRANS results in final diagrams delivered by the X–Y plotter. In spite of its considerable length, TRANS requires modest computer time thanks mainly to the linearity of the perturbation model. Typical computer time was 6270 ms CPU time on a FACOM M-200 TSS service to obtain one Bode diagram curve.

STABILITY CRITERION IN TERMS OF TRANSFER FUNCTION

Under certain spinning conditions, melt spinlines become unstable and develop a severe sustained oscillation in tension and cross-sectional area.[6,14,15] This instability is known as the draw resonance.[1,16]

For a draw resonance to occur, (1) the spinline has to be taken up at a constant speed, (2) ambient air temperature θ^* has to be high enough so that the spinline does not cool down to the solidification temperature of 60°C at the take-up, and (3) the draw ratio $\psi_w = v_w/v_{00}$ must be above a certain critical value. Spinlines in the molten state can be taken up at a constant speed by passing the filament into a water quench bath before taking up.

Kase et al.,[6] Kase,[7] and Kase and Denn[8] stated that a melt spinline is unstable when the vector locus of the transfer function (the present G_2) between spinline tension $\hat{\eta}$ and spinline velocity $\hat{\psi}(\zeta_w, \tau)$ at the take-up distance encircles the origin of the complex plane. This statement, however, was made rather intuitively without full proof. What follows is a proof for the above stability criterion.

As discussed in the preceding section, the transfer function $G(s)$ in eqs. (59) and (60) is for a constant take-up-speed spinline, whereas its four components $G_1(s)$ through $G_4(s)$ are for a constant-tension spinline. For the above constant take-up-speed spinline to be unstable, $G(s)$ must have a pole in the right-hand half of the complex s plane. But none of $G_1(s)$ to $G_4(s)$ have a pole in the right-half s plane since the constant-force spinline is always stable. Then, the only chance $G(s)$ can have a pole in the right-hand half s plane is for $G_2(s)$ to have

a zero in the right-hand half s plane since only $G_2(s)$ consistently appears as denominator.

The above reasoning leads to the statement of the stability criterion: A constant take-up-speed spinline is unstable when the transfer function $G_2(s)$ connecting tension $\hat{\eta}$ to velocity $\hat{\psi}(\zeta_w, \tau)$ has a zero in the right-hand half of the complex s plane.

Further, according to the theories of complex functions, the vector locus $G_2(j\omega)$ encircles the origin of the complex plane Z–P times in the clockwise direction when $G_2(s)$ has Z zeros and P poles in the right-hand half of the s plane, whereas P is known to be equal to zero due to the stability of constant-tension spinline. Therefore, the number of times the $G_2(j\omega)$ locus encircles the origin is equal to Z number of instability causing zeros of $G_2(s)$. This leads to the following alternative expression of the stability criterion: "A constant take-up-speed spinline is unstable when the $G_2(j\omega)$ locus encircles the origin of the complex plane."[6–8] For its geometric nature, this expression of stability criterion is particularly useful in the numerical determination of the conditions of neutral stability.

Figure 7 shows the process in which the response of cross-sectional area $\hat{\xi}(\zeta_w, \tau)$ at constant-speed take-up point to a unit step increase in take-up speed $\hat{\psi}(\zeta_w, \tau)$ changes from stable converging oscillation to unstable diverging oscillation as the ambient air temperature T^* is raised from 20° to 271°C ($\theta^* = 0.074$ to 1.0). Here, the take-up speed is constant in the sense that it remains constant after $\tau = 0$. Figure 8 shows the $G_2(j\omega)/H$ loci corresponding to the four step responses in Figure 7. G_2 was normalized with respect to the zero frequency gain H in eq. (53) for the convenience of graphic presentation. Note that the $G_2(j\omega)/H$ loci for $T^* = 160$ and 271°C encircle the origin to indicate instability.

A Fortran program called MS3ST was developed to automatically search the neutral stability conditions. The MS3 part of MS3ST computes the velocity transient $\psi(\zeta_w, \tau)$ in response to a unit step increase in tension $\hat{\eta}$. The DMS part does the Laplace transformation of the $\hat{\psi}(\zeta_w, \tau)$ to obtain $G_2(j\omega)$. The rest of MS3ST increases the value of a chosen parameter, in this case ambient air

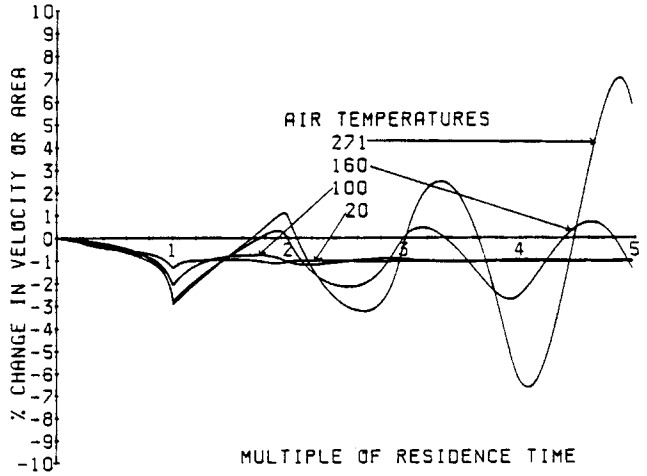

Fig. 7. Response of take-up cross-sectional area to unit step (1%) increase in take-up speed.

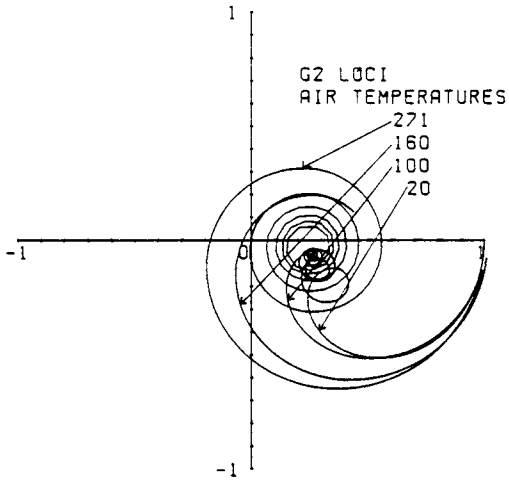

Fig. 8. $G_2(j\omega)/H$ loci for the step responses in Fig. 7.

temperature T^*, until $G_2(j\omega)$ starts to intersect the real axis. Finally, MS3ST modifies the T^* value in a Newton–Raphson iteration scheme until the $G_2(j\omega)$ locus intersects the real axis at the origin to attain neutral stability.

As was shown elsewhere,[6,7,13] the response of the velocity $\hat{\psi}(\zeta_w, \tau)$ to a unit step tension $\hat{\eta}(\tau)$ disturbance in the isothermal spinning of Newtonian fluids has the analytical expression eqs. (61):

$$\hat{\psi}(\zeta_w, \tau) = -\log(1 - \tau \log \psi_w) + \frac{1 - \psi_w^{-1} - \tau \log \psi_w}{1 - \tau \log \psi_w}$$

$$\text{when } 0 < \tau < (1 - \psi_w^{-1})/\log \psi_w = \zeta_w$$

$$\hat{\psi}(\zeta_w, \tau) = \log \psi_w \qquad \text{when } \tau > \zeta_w \tag{61}$$

When the analytical expressions in eqs. (61) were used in place of the numerical transient solution by MS3, the critical draw ratio value in eq. (62) was obtained[8]:

$$\psi_w = 20.218 \tag{62}$$

The above critical draw ratio of 20.218 for an isothermal Newtonian spinline is in approximate agreement with the $e^3 = 20$ given previously by Kase et al.[6] and the 20.21 by Gelder[15] and is estimated to have at least four-digit accuracy.

The counterparts of eq. (61) for spinlines of isothermal power law fluids are[13]

$$\hat{\psi}(\zeta_w, \tau) = \frac{1}{n} + \frac{\psi_w^{1/n-1}}{n-1}\left\{\left(1 - \frac{\psi_w^{1-1/n} - 1}{n-1}\right)^{1-n} - 1\right\} - \frac{\psi_w^{-1}}{n}\left(1 - \frac{\psi_w^{1-1/n} - 1}{n-1}\tau\right)^{-n}$$

$$\text{when } 0 < \tau < \frac{1}{1-n}(1 - \psi_w^{1/n-1}) = \zeta_w$$

$$\hat{\psi}(\zeta_w, \tau) = H = \frac{1 - \psi_w^{1/n-1}}{n-1} \qquad \text{when } \tau > \zeta_w \tag{63}$$

TABLE I
Critical Draw Ratio ψ_w Versus Power Law Exponent n

n	ψ_w	
	Present work	Pearson and Shah, 1974[17]
0.0	1.0[a]	
0.02	1.037	
0.04	1.116	
0.06	1.129	
0.08	1.310	
0.1	1.510	1.51
0.2	2.074	2.09
0.3	2.777	2.785
0.4	3.674	3.67
0.5	4.835	4.83
0.6	6.357	6.37
0.7	8.382	8.43
0.8	11.12	11.35
0.9	14.90	14.68
1.0	20.22[b]	20.20
1.1	27.96	27.99
1.2	39.58	39.73
1.3	57.85	57.84
1.4	88.23	90.04
1.5	142.8	
1.6	252.3	
1.7	512.3	
1.8	1340	
1.9	6456	
2.0	[a]	

[a] Derived analytically in eqs. (66) and (68).
[b] Due to eq. (61).

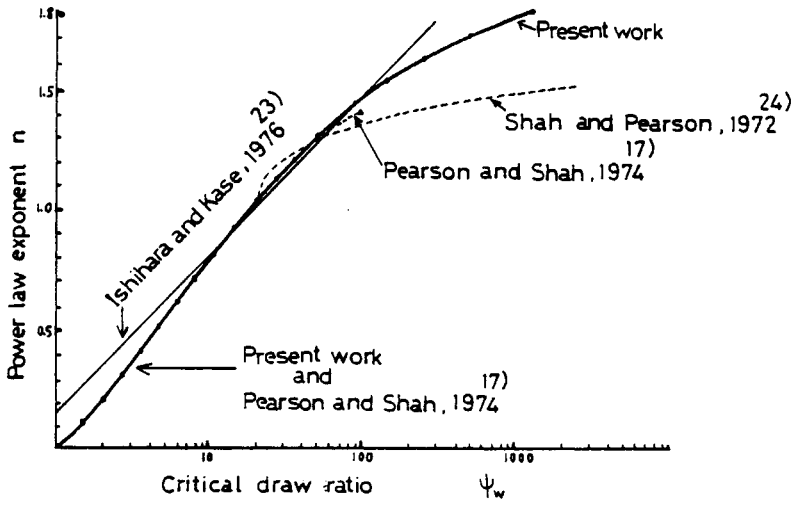

Fig. 9. Critical draw ratio ψ_w vs. power law exponent n.

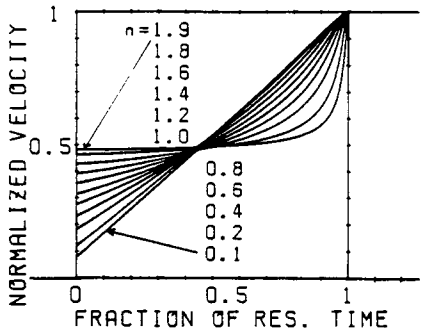

Fig. 10. Transient response of spinline velocity $\hat{\psi}(\zeta_w, \tau)$ to unit step increase in tension $\hat{\eta}(\tau)$ under the draw ratio–power law exponent combinations given in Table I.

The analytical expression of velocity response $\hat{\psi}(\zeta_w, \tau)$ in eqs. (63) was used in a program called PLW, similar in construction to MS3ST, to compute the critical draw ratio ψ_w under different values of power law exponent n, with the results shown in Table I and Figure 9. The presently obtained $\psi_w(n)$ relation is in precise agreement with the previous values obtained by Pearson and Shah[17] using eigen value approach to demonstrate the equivalence of the two methods.

Figure 10 shows the step responses $\hat{\psi}(\zeta_w, \tau)/H$ vs. time τ/ζ_w as given in eq. (63) and under the neutral stability conditions shown in Figure 9 and Table I. The normalization of $\hat{\psi}$ and τ with respect to the final H value and steady-state residence time ζ_w is irrelevant to stability. It is quite interesting to find in Figure 10 that in the limit of $n = 0$, the transient $\hat{\psi}/H$ in Figure 10 becomes a ramp and, in the limit of $n = 2.0$, $\hat{\psi}/H$ tends to a staircase shape. In fact, eq. (63) yields

$$\lim_{\psi_w \to \infty} [\hat{\psi}(\zeta_w, \tau)/H] = 1 - \frac{1}{n} \qquad \text{when } 0 < \tau/\zeta_w < 1 \tag{64}$$

$$\lim_{\psi_w \to 0} [\hat{\psi}(\zeta_w, \tau)/H] = \tau/\zeta_w \qquad \text{when } 0 < \tau/\zeta_w < 1 \tag{65}$$

The staircase-shape step response given in eq. (64) is equivalent to the analytical expression of $G_2(s)$ in eq. (66) below when normalized time τ/ζ_w is used rather than time τ:

$$\frac{G_2(s)}{H} = \left(1 - \frac{1}{n}\right) + \frac{e^{-s}}{n} \tag{66}$$

The $G_2(j\omega)/H$ locus in eq. (66) passes through the origin of the complex plane when n is equal to 2.0. Therefore, spinlines of isothermal power law fluids are neutrally stable when

$$\psi_w = \infty \qquad \text{and} \qquad n = 2 \tag{67}$$

indicating that the $\psi_w(n)$ curve in Figure 9 tends to $\psi_w = \infty$ as n approaches 2.0.

The $G_2(s)$ for the ramp-shaped step response $\hat{\psi}(\zeta_w, \tau)$ in eq. (65) is

$$\frac{G_2(s)}{H} = \frac{1 - e^{-s}}{s} \tag{68}$$

The $G_2(j\omega)/H$ locus for eq. (68) above always passes through the origin of the

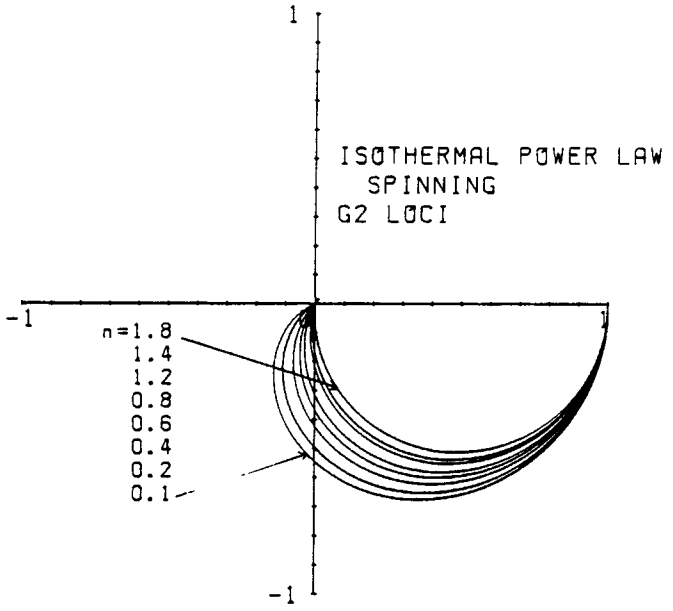

Fig. 11. $G_2(j\omega)/H$ loci for the step responses in Fig. 10.

complex plane. Therefore, the $\psi_w(n)$ curve in Figure 9 should pass through the

$$\psi_w = 1 \qquad \text{and} \qquad n = 0 \tag{69}$$

point. The above two points given in eqs. (67) and (69) supplements the $\psi_w(n)$ curve first given by Pearson and Shah.[17]

Figure 11 shows the $G_2(j\omega)/H$ loci under the neutral stability conditions given

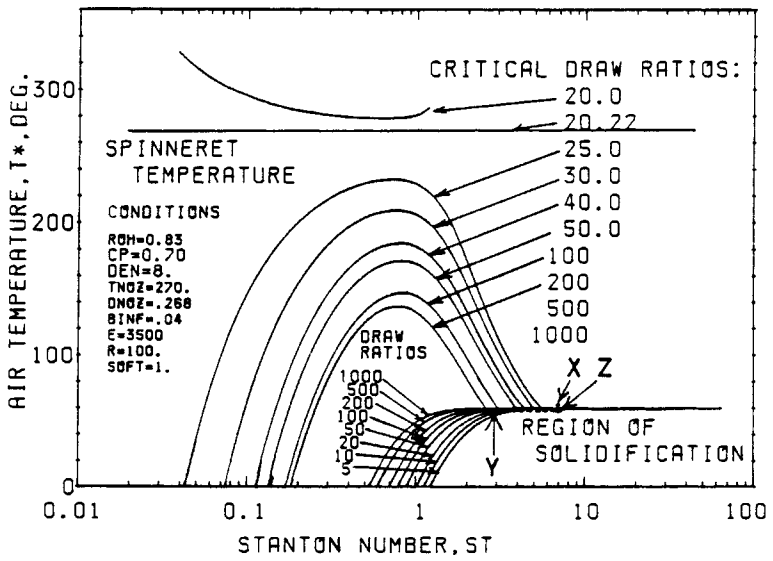

Fig. 12. Neutral stability map on the air temperature T^* vs. Stanton number St plane.

in Table I. All loci in Figure 11 pass through the origin to confirm the neutral stability attained by program PLW.

Shown in Figure 12 are contours of constant critical draw ratio ψ_w for ranges of ambient air temperatures T^* and Stanton numbers St computed by program MS3ST and drawn by its graphic routine. Figure 12 is essentially identical to Figures 9 and 16 of Kase,[7] except that many critical draw ratio values are now given instead of just one such value and that the curves are much more accurate than those in Kase.[7] Parameter values used in Figure 12 except for T^* are given as eqs. (41) and (42).

The stability map in Figure 12 consists of two groups of curves. The parabolalike peak-forming group of curves are the ones first discovered by Shah and Pearson[18] with the spinline stable in the region below each of these curves. The second group of curves leveling off at 60°C are the limits of the region in which the spinline solidifies prior to take-up. When solidification occurs, the spinline is known to be always stable.[7,19]

Moving horizontally within the above region of solidification is equivalent to merely changing the length of the solidified part of the spinline without any real change in the dynamics of the molten upper part.[7,20] Therefore, a very small downward movement across the 60°C solidification boundary LM from point Z to point X in Figure 12 is equivalent to moving all the way from Z to Y. Evidently, point Y, which is horizontally left of X and on the solidification boundary, is deep in the midst of the very stable region below the first group of curves. Thus, we know that a very sudden change in the state of the spinline from very unstable to very stable takes place in crossing the solidification limit LM from Z to X. In fact, the high stability of industrial melt spinning can be attributed to this very strong stabilizing effect of solidification since industrial melt spinning usually operates outside the above first group of curves but below the solidification boundary LM.

The three $G_2(j\omega)/H$ loci shown in Figure 13 demonstrate the dramatic sta-

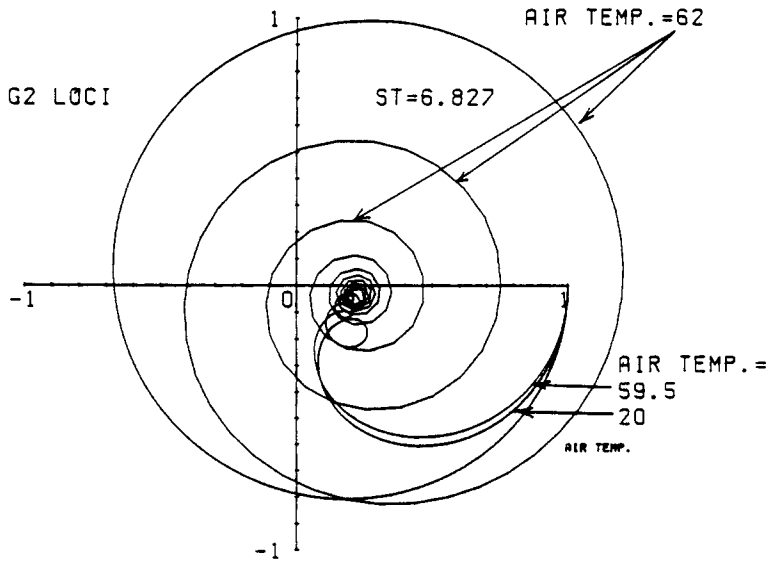

Fig. 13. $G_2(j\omega)/H$ loci for points W, X, and Z in Fig. 12.

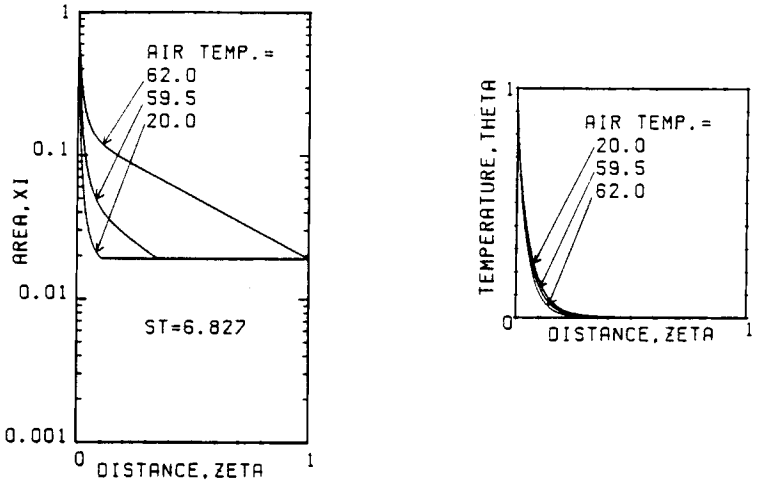

Fig. 14. Steady-state area and temperature profiles for points W, X, and Z in Fig. 12.

bilization of the spinline as the air temperature drops by a mere 2.5° from 62° to 59.5°C to cross LM while keeping St unchanged at 6.827. The $G_2(j\omega)$ loci for $T^* = 20$ and 59.5°C are quite similar in shape and do not encircle the origin to show that the spinline is stable, whereas the $G_2(j\omega)$ locus for $T^* = 62$°C is very much different in shape and makes three big encirclements of the origin to show a highly unstable spinline. The three steady-state solutions shown in Figure 14 correspond to the three $G_2(j\omega)$ loci in Figure 13. The very sudden stabilization of spinline occurring in crossing LM must be due to the abrupt change in steady-state area profile as shown in Figure 14 brought about by the appearance of solidification, since coefficients f_1 through f_6 of the perturbation equations are determined solely by the steady-state solution.

While the physical mechanism that causes the draw resonance instability has been discussed in various ways,[1,6,7,14,15,21] the results of this section show quite clearly that draw resonance is caused by an instability occurring in the control system which forces the spinline to satisfy the downstream boundary condition of constant take-up speed by means of an information feedback through time varying tension.

SENSITIVITY

While spinline instability presents an interesting theoretical subject, its industrial implications are quite limited since draw resonance is rarely encountered in production sites, with the chill roll casting of polypropylene film being probably the only exception.

On the other hand, industrial melt spinning is always subject to unavoidable external disturbances such as fluctuating cooling air speed $\hat{\psi}_y$ or extrusion viscosity, resulting in filament unevenness. This makes the sensitivity of spinlines to disturbances a practical concern, and this is where transfer function analysis is quite useful.

In sensitivity analysis, it is convenient to measure the variation of each variable in percentage deviation from the steady-state value. As eq. (A-5) shows, a sinusoidal disturbance input of 1% amplitude given to the spinline produces a si-

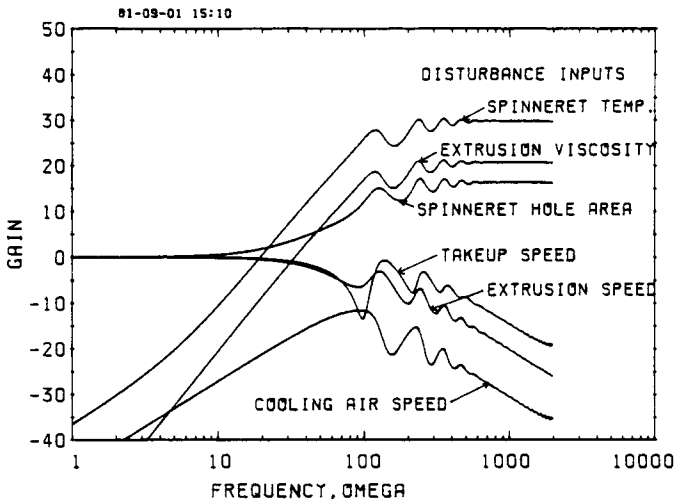

Fig. 15. Frequency response of take-up cross-sectional area to six different disturbance inputs under constant take-up speed expressed as Bode gain diagrams (gain).

nusoidal change in output variable having the same frequency and an amplitude of $|G(j\omega)|$ %. This makes the Bode gain diagram, the plot of $20 \log_{10}|G(j\omega)|$, a good quantitative measure of the effects of disturbance.

The six Bode gain diagrams in Figure 15 show the effects of six different disturbance inputs upon the cross-sectional area $\hat{\xi}(\xi_w, \tau)$ at the constant speed take-up roll. The computation and graphics are due to program TRANS. Figure 16 shows corresponding Bode angle diagrams. Parameter values used are as given in eqs. (41) and (42).

The gain diagram for spinneret hole area input $\hat{\xi}(0, \tau)$ starts at zero gain and levels off in the high-frequency range at a gain value approximately equal to 16. A zero gain means that a sinusoidal change in spinneret hole area by an amplitude of 1% of the steady-state value results in a sinusoidal change in cross-sectional

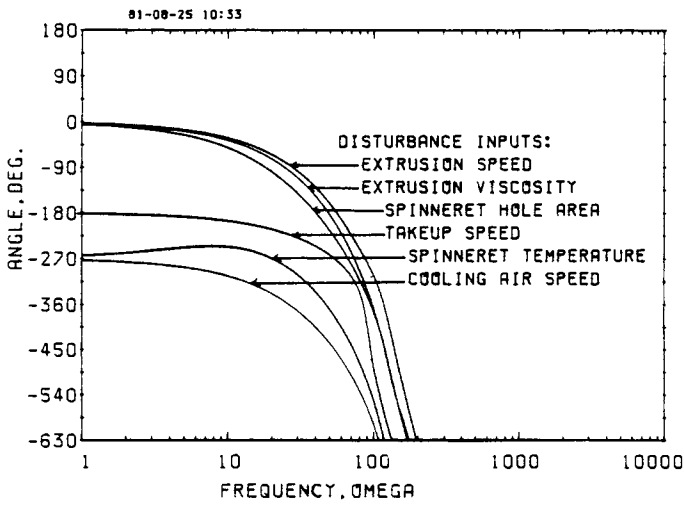

Fig. 16. Bode angle diagrams corresponding to Fig. 15.

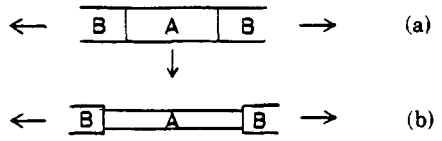

Fig. 17. Formation of dent in stretching a cylindrical filament having lengthwise viscosity variation.

area at take-up by an amplitude of 1%. In the high-frequency end, 1% input amplitude produces $10^{16/20} = 6.31\%$ output amplitude, an amplification of 6.3 times.

The gain diagrams in Figure 15 for take-up speed input $\hat{\psi}(\zeta_w, \tau)$, extrusion speed input $\hat{\psi}(0, \tau)$, and spinneret hole area input go to zero gain at low frequencies, since very slowly increasing any one of the three input variables by 1%, keeping other conditions unchanged, will result in a +1 or −1% change in take-up cross-sectional area.

It is quite significant that with the three disturbance inputs—spinneret temperature $\hat{\theta}(0, \tau)$, spinneret hole area, and extrusion viscosity $\hat{\beta}(\tau)$—the gain diagram levels off at a high gain value as frequency goes to infinity. An input amplitude of 1% in extrusion viscosity, for instance, results in a take-up area amplitude of $10^{21/20} = 11.2\%$, an amplification of disturbance by a factor of 11.2 at high frequencies. This means that when the polymer extruded from the spinneret contains very fine particles of slightly different viscosity, a considerable filament unevenness is predicted to result. In fact, this effect can be explained by a very simple physical model.

Suppose a fluid filament of uniform thickness consists of three sections in tandem connection as shown in Figure 17(a). The three sections consist of fluids B, A, and B, respectively, and fluid A is lower in viscosity than fluid B. When this filament is extended, the low-viscosity A part thins out faster than the B part to develop a square-dent unevenness. The depth of the dent increases with increasing draw ratio. In fact, this is the very mechanism which produces the area discontinuity shown in Figures 3 and 5 and in eqs. (43) to (50). Furthermore,

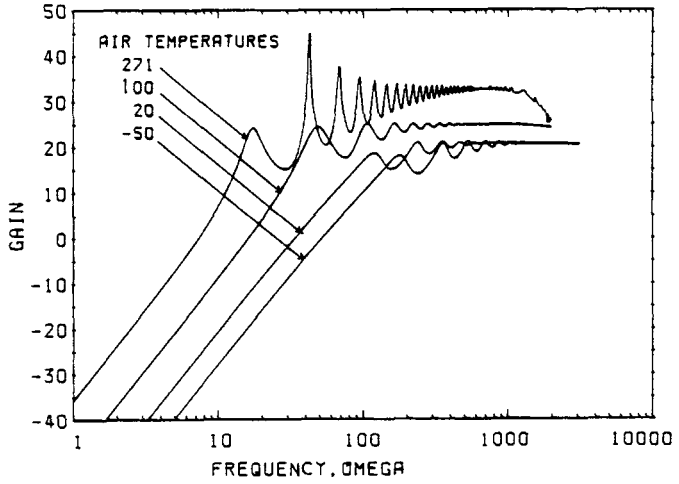

Fig. 18. Frequency response of take-up cross-sectional area to extrusion viscosity disturbance under different air temperatures.

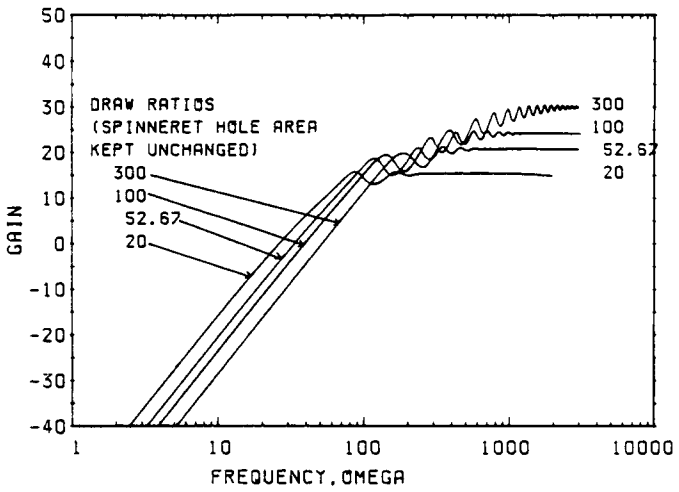

Fig. 19. Frequency response of take-up cross-sectional area to extrusion viscosity disturbance under different spinneret hole areas.

it can be shown that the discontinuity or jump in $\hat{\xi}(\zeta_w, \tau)$ at $\tau/\zeta_w = 1$ in Figure 3 makes the $G(j\omega)$ locus tend to a transportation lag circle whose center coincides with the origin. This is the reason why the gain diagram for extrusion viscosity input in Figure 15 tends to a large fixed value in the limit of infinite frequency. Thus, we know that a high-frequency viscosity variation at the spinneret can be the cause of considerable filament irregularity.

In practice, spinneret temperature is insignificant as a disturbance input since the large heat capacity of the spinneret block makes high-frequency temperature changes unlikely. So is spinneret hole area input, because quick changes in hole area are not likely to occur in practice, except in the case of clogging, which usually renders the spinneret hole useless anyway.

The gain diagram is attenuated in the high-frequency range under the three disturbance inputs, take-up speed, extrusion speed, and cooling air speed, probably because the spinline tends to damp these disturbances.

The effect of cooling air speed variation $\hat{\psi}_y$ is surprisingly small. Even at its peak, the gain is as low as -12 to make a 1% sinusoidal variation in $\hat{\psi}_y$ cause a mere $10^{-12/20} = 0.25\%$ sinusoidal variation in take-up cross area. In view of the above findings, the authors strongly suspect that whatever thickness variations are present in industrially melt-spun undrawn filaments are due primarily to variations in the quality of the polymer emerging from the spinneret hole.

Shown in Figure 18 are Bode gain diagrams for the effect of extrusion viscosity variation on take-up cross area variation under different ambient air temperatures T^*. Increasing T^* not only makes the spinline unstable, as shown in Figures 7, 8, and 12, but also makes the spinline more sensitive to external disturbances. We can then conclude that the role of air cooling of the spinline is to stabilize the spinline and at the same time make it less sensitive to external disturbances.

Figure 19 shows the Bode gain diagrams for the effect of extrusion viscosity on take-up cross area under different spinneret hole areas. Increasing the steady-state drawdown ratio by enlarging the spinneret hole keeping other conditions unchanged evidently has the adverse effect of making the spinline

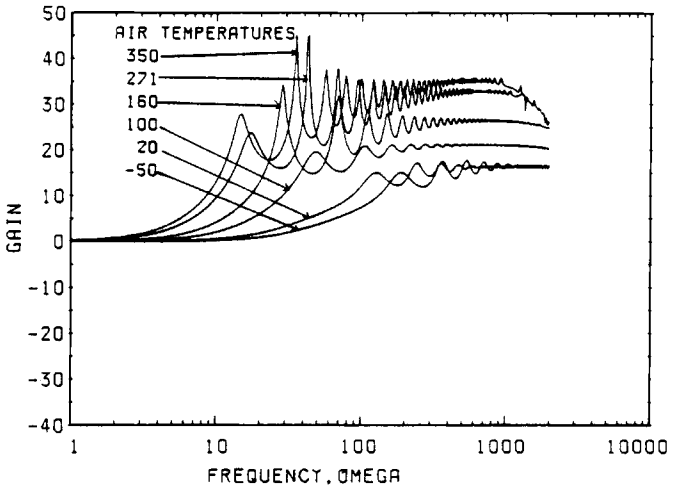

Fig. 20. Frequency response of take-up cross-sectional area to spinneret hole area disturbance under different air temperatures.

increasingly sensitive to disturbances in the high-frequency range. This is consistent with the common field experience that large drawdown ratios are conducive to uneven filaments.

Figure 20 shows the response of take-up cross-sectional area to spinneret hole area disturbance input under different cooling air temperatures. Here again, increasing the air temperature quickly increases the sensitivity of the spinline in the high-frequency range.

Shown in Figure 21 is the response of take-up cross-sectional area to cooling-air speed disturbance under different air temperatures. Increasing the air temperature increases spinline sensitivity mainly in the vicinity of the characteristic frequency of the spinline. When the air temperature approaches the spinneret temperature of 270°C, however, the sensitivity suddenly decreases toward zero. This is because cooling-air speed variation can affect the spinline only through

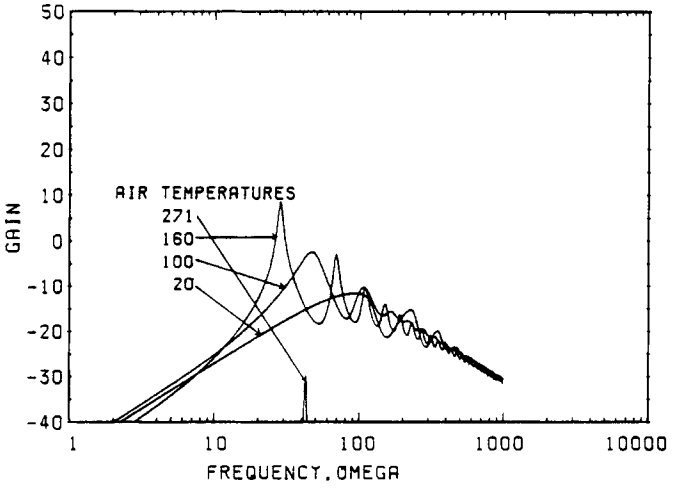

Fig. 21. Frequency response of take-up cross-sectional area to cooling-air speed disturbance under different air temperatures.

heat transfer, and it tends to zero as the air temperature approaches the spinneret temperature.

CONCLUSIONS

A formal proof was given of the criterion of spinline stability stated in terms of transfer function.

A systematic procedure to express the dynamical characteristics of spinline in the form of the frequency response Bode diagrams was established, and so was a procedure to accurately compute the conditions of neutral stability of the spinline. These procedures were materialized in three computer programs—TRANS, MS3ST, and PLW—which contain computer graphic routines for the automatic drawing of Bode diagrams and neutral stability maps. In all cases, computer time requirements turned out to be modest.

The authors would like to express their thanks to Professor M. M. Denn of the University of California, Berkeley, for helpful discussions.

APPENDIX

TRANSFER FUNCTION

In this appendix, basics of transfer function are reviewed to provide a background for the discussions in the main text.

Transfer function, usually denoted $G(s)$, is treated in practically all text books of control engineering and is defined as the ratio of the Laplace transform of output signal $y(\tau)$ emerging from a linear system over the Laplace transform of corresponding input signal $z(\tau)$ entering the linear system (see Fig. 22):

$$Z(sd) = \mathcal{L}\{z(\tau)\} = \int_0^\infty e^{-s\tau} z(\tau)\, d\tau \tag{A-1}$$

$$Y(s) = \mathcal{L}\{y(\tau)\} = \int_0^\infty e^{-s\tau} y(\tau)\, d\tau \tag{A-2}$$

$$G(s) = \frac{Y(s)}{Z(s)} \tag{A-3}$$

$G(s)$ is a complex function of the complex variable s and has at least one pole in the right-hand half of the complex s plane when the linear system is unstable.

When the s is replaced with imaginary angular frequency $j\omega$, $G(j\omega)$ gives the frequency response of the linear system. That is to say, when the input signal entering the system is

$$z(\tau) = \sin \omega\tau \tag{A-4}$$

the resultant output signal emerging from the system is expressed as

$$y(\tau) = |G(j\omega)| \sin\{\omega\tau + \angle G(j\omega)\} \tag{A-5}$$

after the initial transients have subsided. The absolute value $|G(j\omega)|$ and angle $\angle G(j\omega)$ are given by the relation

$$\begin{aligned} G(j\omega) &= |G(j\omega)| e^{j\angle G(j\omega)} \\ &= |G(j\omega)| \{\cos \angle G(j\omega) + j \sin \angle G(j\omega)\} \\ &= R\{G(j\omega)\} + jI\{G(j\omega)\} \end{aligned} \tag{A-6}$$

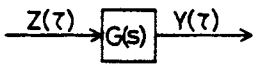

Fig. 22.

The vector locus of $G(j\omega)$ is the locus of vector $G(j\omega)$ drawn on the complex plane when the angular frequency ω is varied continuously from zero to plus infinity.

The Bode diagram of $G(j\omega)$ is usually drawn on a semilog graph paper by taking the angular frequency ω on the semilog x axis and the gain defined as $20 \log_{10}|G(j\omega)|$ and the angle $\angle G(j\omega)$ on the regular-scale y axis.

Furthermore, when the input signal $z(\tau)$ and the resultant output signal $y(\tau)$ are random time functions satisfying ergodicity,[22] the statistical attributes of $z(\tau)$ and $y(\tau)$ can be represented by their respective autocorrelation functions $\phi_{zz}(u)$ and $\phi_{yy}(u)$ defined below:

$$\phi_{zz}(u) = \lim_{T\to\infty} \frac{1}{2T} \int_{-T}^{T} z(\tau)\, z(\tau + u)\, d\tau \tag{A-7}$$

$$\phi_{yy}(u) = \lim_{T\to\infty} \frac{1}{2T} \int_{-T}^{T} y(\tau)\, y(\tau + u)\, d\tau \tag{A-8}$$

When $z(\tau)$ and $y(\tau)$ are the deviations of cooling air speed and the resultant filament cross-sectional area, respectively, from their steady-state values, then $\phi_{zz}(0)$ and $\phi_{yy}(0)$ are the mean square deviations in cooling air speed and filament cross-sectional area, respectively.

Power density spectra $\Phi_{zz}(s)$ and $\Phi_{yy}(s)$, defined below in eqs. (A-9) and (A-10), are the two-sided Laplace transforms of $\phi_{zz}(u)$ and $\phi_{yy}(u)$:

$$\Phi_{zz}(s) = \int_{-\infty}^{\infty} {}_{zz}(u)\, e^{-su}\, du \tag{A-9}$$

$$\Phi_{yy}(s) = \int_{-\infty}^{\infty} {}_{yy}(u)\, e^{-su}\, du \tag{A-10}$$

$\Phi_{yy}(s)$ can be derived from the $\Phi_{zz}(s)$ by the relation (A-11):

$$\Phi_{yy}(j\omega) = |G(j\omega)|^2\, \Phi_{zz}(j\omega) \tag{A-11}$$

Once $z(\tau)$ and $G(j\omega)$ are given, eqs. (A-7), (A-9), and (A-11) enable the computation of $\Phi_{yy}(j\omega)$, which in turn can be used in the inverse Laplace transform below to yield

$$\phi_{yy}(u) = \frac{1}{2\pi} \int_{-\infty}^{\infty} {}_{yy}(j\omega)\, e^{ju\omega}\, d\omega \tag{A-12}$$

$$\phi_{yy}(0) = \frac{1}{2\pi} \int_{-\infty}^{\infty} \Phi_{yy}(j\omega)\, d\omega \tag{A-13}$$

where $\phi_{yy}(0)$ is the predicted mean square filament unevenness due to the disturbance input $z(\tau)$.

References

1. C. J. S. Petrie and M. M. Denn, *AIChE J.*, **22**(2), 209 (1976).
2. M. M. Denn, *Ann. Rev. Fluid Mech.*, **12**, 365 (1980).
3. J. L. White and Y. Ide, *J. Appl. Polym. Sci.*, **22**, 3057 (1978).
4. A. Ziabicki, *Fundamentals of Fiber Formation*, Wiley, New York, 1976.
5. C. J. S. Petrie, *Extensional Flows*, Pitman, London, 1979.
6. S. Kase, T. Matsuo, and Y. Matsuo, and Y. Yoshimoto, *Seni Kikai Gakkaishi*, **19**, T63 (1966).
7. S. Kase, *J. Appl. Polym. Sci.*, **18**, 3279 (1974).
8. S. Kase and M. M. Denn, *Proc. 1978 Joint Automatic Control Conf.*, II-71, (1978).
9. M. M. Denn, in *Computers in Polymer Processing*, J. R. A. Pearson and S. M. Richardson, eds., to be published, 1982.
10. S. Kase and T. Matsuo, *J. Appl. Polym. Sci.*, **11**, 251 (1967).
11. H. H. George, presented at Second Joint U.S.–Japan Soceity of Rheology Meeting, Kona, Hawaii, April 1979.
12. S. Kase and T. Matsuo, *J. Polym. Sci. Part A*, **3**, 2541 (1965).
13. S. Kase, Y. Oki and J. Katsui, *Ind. Eng. Chem. Fundam.*, submitted.
14. J. R. A. Pearson and M. A. Matovich, *Ind. Eng. Chem. Fundam.*, 8(4), 605 (1969).
15. D. Gelder, *ibid.*, **10**(3), 534 (1971).

16. J. C. Miller, *SPE Trans.*, **3**, 134 (1963).
17. J. R. A. Pearson and Y. T. Shah, *Ind. Eng. Chem. Fundam.*, **13**(2), 134 (1974).
18. Y. T. Shah and J. R. A. Pearson, *ibid.*, **11**(2), 145 (1972).
19. J. R. A. Pearson, Y. T. Shah, and R. D. Mhaskar, *ibid.*, **15**(1), 31 (1976).
20. J. C. Chang, M. M. Denn and S. Kase, *ibid.*, **21**(1), 13 (1982).
21. J. C. Hyun, *AIChE J.*, **20**(3), 418 (1978).
22. J. C. Truxal, *Automatic Feedback Control System Synthesis*, McGraw-Hill, New York, 1955.
23. H. Ishihara and S. Kase, *J. Appl. Polym. Sci.*, **20**, 169 (1976).
24. Y. T. Shah and J. R. A. Pearson, *Ind. Eng. Chem. Fundam.*, **11**, 145 (1972).

Received April 19, 1982
Accepted June 1, 1982